

# Optical Second- and Third-Order Nonlinearities in Plasma-Enhanced Chemical Vapor Deposition-Grown Silicon Oxides and Silicon Nitrides

Laurids Wardenberg,\* André Kühling, and Jörg Schilling

Optical second- and third-order nonlinearities ( $\chi^{(2)}$  and  $\chi^{(3)}$ ) in nonstoichiometric silicon oxides and silicon nitrides grown by plasma-enhanced chemical vapor deposition are investigated by second-harmonic generation (SHG) and electric field-induced second-harmonic (EFISH) measurements. The free-space SHG measurements with a fundamental wavelength of 1030 nm allow us to determine the bulk  $\chi^{(2)}$  values of both material platforms for various material compositions. It is demonstrated that the bulk  $\chi^{(2)}$  values can be strongly enhanced by increasing the silicon content, reaching maximum values of the main  $\chi^{(2)}$  tensor component of  $\chi_{zzz}^{(2)} = 6.8 \text{ pm V}^{-1}$  for silicon-rich nitrides and  $\chi_{zzz}^{(2)} = 8.0 \text{ pm V}^{-1}$  for silicon-rich oxides. EFISH measurements demonstrate that the  $\chi^{(2)}$  values can be pushed even further by adding a static electric field to the materials. Similar to the  $\chi^{(2)}$  values, the  $\chi^{(3)}$  values are strongly enhanced by increasing the silicon content, leading to a maximum  $\chi_{zzzz}^{(3)}$  value of  $\approx 0.5 \times 10^{-18} \text{ m}^2 \text{ V}^{-2}$  for the silicon-rich nitrides and  $\approx 1.0 \times 10^{-18} \text{ m}^2 \text{ V}^{-2}$  for the silicon-rich oxides.

## 1. Introduction

As a complementary metal-oxide semiconductor (CMOS)-compatible material platform with its advantageous optical properties, such as high refractive index and low losses in the IR spectral region, silicon nitride is widely used for passive integrated photonic structures, for example, low-loss waveguides, Mach-Zender interferometers, and ring resonators.<sup>[1–4]</sup> Besides that, the sizeable but rather unexpected optical second-order nonlinearity ( $\chi^{(2)}$ ) of silicon nitride grown by plasma-enhanced chemical vapor deposition (PECVD) has been known for more than a decade and has gained a lot of interest in the years

following its discovery.<sup>[5–8]</sup> The linear and nonlinear optical properties can be tuned by changing the deposition parameters of the PECVD process.<sup>[6,7]</sup> Here, the gas flow ratios of the precursor gases  $\text{SiH}_4$ ,  $\text{NH}_3$ , and  $\text{N}_2$  play a key role for the resulting optical properties. In general, a higher fraction of  $\text{SiH}_4$  in the used gas mixture leads to a higher fraction of silicon in the deposited silicon nitride. PECVD-grown silicon-rich nitride (SRN) exhibits an increased refractive index and stronger absorption in the visible and near-IR region compared to stoichiometric silicon nitride ( $\text{Si}_3\text{N}_4$ ).<sup>[9,10]</sup> In addition, it has been shown that a higher refractive index is associated with an enhanced optical second-order nonlinearity in SRN.<sup>[6,7]</sup> Besides the peculiar second-order nonlinearity, SRN exhibits a large classic third-order nonlinearity ( $\chi^{(3)}$ ) up to  $10^{-18} \text{ m}^2 \text{ V}^{-2}$ , comparable to that of

silicon.<sup>[11–16]</sup> These second- and third-order nonlinear properties expand the field of applications of SRN from passive structures to active structures capable of manipulating the wavelength of light, such as second-harmonic generation (SHG) and third-harmonic generation (THG) in waveguides and ring resonators, four-wave mixing (FWM), supercontinuum generation, and parametric down-conversion.<sup>[16–22]</sup> Moreover, the large third-order nonlinearity can be utilized to further control and enhance the  $\chi^{(2)}$  by applying a static electric field to the material.<sup>[7,11]</sup> This so-called electric field-induced second-harmonic generation (EFISH) effect connects the applied static electric field strength  $E_{\text{DC}}$  with the  $\chi^{(3)}$  of the material to create a quasi- $\chi^{(2)}$

$$\chi_{\text{quasi}}^{(2)} = 3\chi^{(3)}E_{\text{DC}} \quad (1)$$

With this method a maximum  $\chi^{(2)}$  value of multiple  $10 \text{ pm V}^{-1}$  was achieved in SRN.<sup>[7]</sup> Most studies targeting the topic of tunable nonlinearities are limited to SRN with a refractive index of  $n \leq 2.2$  in the near infrared.<sup>[6,7,23]</sup> In this work we expand the investigations of the material platform to silicon-rich nitrides with refractive indices up to  $n \lesssim 2.7$  to test the limits of the achievable  $\chi^{(2)}$  and to give a complete overview from nitrogen-rich silicon nitride to high-refractive-index SRN. Furthermore, we apply the same concept to PECVD-grown silicon oxides, a so-far mostly unexplored material platform for effective SHG and EFISH applications, which has been shown

L. Wardenberg, A. Kühling, J. Schilling


Department of Physics

Martin-Luther-University Halle-Wittenberg

Karl-Freiherr-von-Fritsch-Straße 2, 06120 Halle(Saale), Sachsen-Anhalt,

Germany

E-mail: laurids.wardenberg@physik.uni-halle.de

 The ORCID identification number(s) for the author(s) of this article can be found under <https://doi.org/10.1002/adpr.202400142>.

© 2024 The Author(s). Advanced Photonics Research published by Wiley-VCH GmbH. This is an open access article under the terms of the Creative Commons Attribution License, which permits use, distribution and reproduction in any medium, provided the original work is properly cited.

DOI: 10.1002/adpr.202400142

to exhibit third-order nonlinearities similar to those of SRN.<sup>[24]</sup> Compared to silicon nitride, silicon oxides have the advantage of an even larger refractive index tuning range extending also to lower refractive indices of  $n > 1.45$ . Our SHG and EFISH measurements allow the determination and direct comparison of the second- and third-order nonlinearities of both material platforms using the same deposition and characterization method. This demonstrates the novel finding that silicon nitride is not the only PECVD-grown material exhibiting sizeable optical second-order nonlinearities and might indicate that PECVD itself is a potentially interesting tool for creating various second-order nonlinear materials.

## 2. Experimental Section

All samples consisted of a fused silica substrate coated with a PECVD-grown material, either silicon nitride or silicon oxide. For the deposition of silicon nitride, we used a PECVD recipe with  $\text{SiH}_4$ ,  $\text{NH}_3$ , and  $\text{N}_2$  as precursor gases, where the total gas flow and the flow of  $\text{N}_2$  were fixed at 1000 and 950 sccm, respectively. The flowrate ratio of  $\text{SiH}_4$  and  $\text{NH}_3$  was then varied to create silicon nitrides with various silicon fractions, for example, a ratio of 1:1 leads to stoichiometric silicon nitride. The depositions were processed at a temperature of 300 °C, a pressure of 500 mTorr, and radiofrequency (RF) power of 50 W. To deposit silicon oxide, different PECVD process parameters were used. As precursor gases we used  $\text{SiH}_4$ ,  $\text{N}_2\text{O}$ , and Ar. The total gas flow and the flow of  $\text{SiH}_4$  were fixed at 1080 and 45 sccm, respectively. To tune the silicon fraction of the silicon oxides, the ratio of  $\text{SiH}_4$  and  $\text{N}_2\text{O}$  was changed by varying the flow of  $\text{N}_2\text{O}$ . To maintain a total gas flow of 1080 sccm the flow of Ar was adjusted accordingly. Other process parameters were the temperature of 300 °C, the pressure of 500 mTorr, and the RF power of 13 W. The PECVD-grown films were investigated by ellipsometry to obtain basic properties such as layer thickness and the refractive index. The results are shown in Figure 1. The thicknesses of the deposited films were in the range of 100–1600 nm.

For EFISH measurements, where a static electric field was applied to the investigated material while measuring the SHG intensity simultaneously, electrodes were added to the sample design. For that purpose, we coated the fused silica substrate with a 4 nm thin layer of chromium before we added the PECVD-grown material. After deposition of the silicon oxide or silicon nitride, we coated another layer of 4 nm chromium on top by sputter deposition. This led to a structure where the material under study was sandwiched between the two chromium electrodes and it allowed to apply a homogeneous static electric field to it (see Figure 2). Note that the chromium layers acted as semitransparent electrodes.

## 3. Free-Space Measurements

To characterize the optical nonlinear properties of PECVD-grown silicon nitride and silicon oxide, we perform free-space SHG and EFISH measurements. For both types of measurements, the same setup is used, but the sample design differs (see section 2). A Yb:KGW laser with a wavelength of 1030 nm, a pulse duration of 180 fs, and a repetition rate of 1 kHz is used as the source for the fundamental beam. We used an average power of 100 mW, which corresponds to a peak power of  $\approx 1$  GW. The setup includes a half-wave plate, a polarizer, and a 1030 nm bandpass filter before the sample and multiple 515 nm bandpass filters and a polarizer behind the sample (see Figure 3). The 1030 nm bandpass filter suppresses potential SHG light mixed in with the fundamental beam before reaching the sample, while the combination of the half-wave plate and the polarizer allows to change the linear polarization direction and power of the fundamental beam. The multiple 515 nm bandpass filters behind the sample separate the SHG and fundamental beams by suppressing the fundamental beam and transmitting the SHG beam emitted from the sample. The second polarizer determines the polarization direction of the measured SHG signal. In the following, we refer to the polarization configuration of the fundamental and the SHG beam as s-s, s-p, p-s, or p-p, where the first letter describes the polarization of the incident fundamental beam

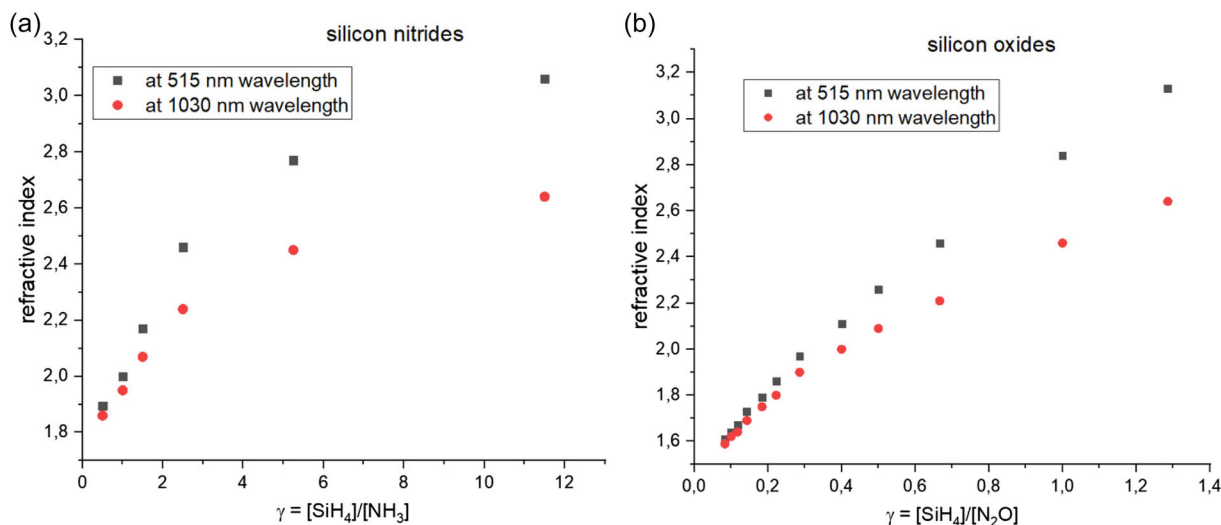


**Figure 1.** Refractive indices of the a) PECVD-grown silicon nitrides and b) silicon oxides at the fundamental wavelength 1030 nm and the SHG wavelength 515 nm.

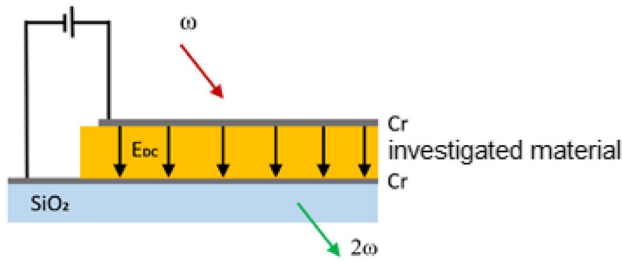


**Figure 2.** Schematic image of the sample design for EFISH measurements. Reproduced with permission.<sup>[33]</sup> Copyright 2024, Optica Publishing Group.

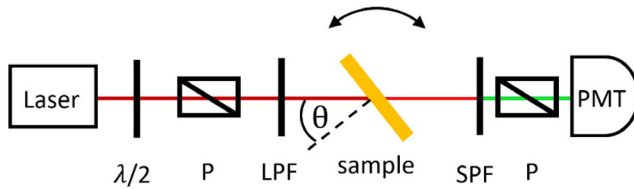


**Figure 3.** Schematic image of the setup used for SHG and EFISH measurements. The half-wave plate in combination with a polarizer (P) allows to adjust the intensity and polarization direction of the fundamental beam, long-pass filter, and short-pass filter separate pump and SHG radiation prior to sending the SHG beam through an analyzer (P) into the detector (PMT). Reproduced with permission.<sup>[33]</sup> Copyright 2024, Optica Publishing Group.

and the second letter the polarization of the created SHG beam, for example, p-s means p-polarized fundamental beam and s-polarized SHG beam out. For each measurement, the polarization stays fixed. The sample, located between the two different bandpass filters, is mounted on a rotation stage to allow to vary the angle of incidence during the measurements. The SHG signal is finally detected by a photomultiplier.

### 3.1. SHG Measurements

First, the SHG measurements are carried out on the samples with PECVD-grown materials on fused silica substrates without

chromium electrodes. The SHG intensity is measured while rotating the sample and therewith changing the angle of incidence from  $-60^\circ$  to  $+60^\circ$ . A typical result is shown in **Figure 4a,b**. Besides the angle of incidence, the measured SHG intensity depends significantly on the polarization configuration. For s-p and p-p configuration, an SHG signal is detected, while for s-s and p-s configuration the SHG signal vanishes. This is the case for all silicon nitride and silicon oxide samples and is a strong indication that all films exhibit an in-plane isotropy (symmetry group  $C_{\infty v}$ ). This finding matches very well with the results in the literature.<sup>[5–8]</sup>

### 3.2. EFISH Measurements

To perform EFISH measurements, the samples with additional chromium electrodes are used. The angle of incidence stays fixed at  $22.5^\circ$  for all measurements while the applied static electric field is varied. Similar to the SHG measurements, no s-polarized SHG was observed for all polarization configuration, indicating that in-plane isotropy remains preserved. This is the case for all silicon nitride and silicon oxide samples. Since the SHG intensity  $I_{\text{SHG}}$  is proportional to the square of  $\chi^{(2)}$ , according to Equation (1), this leads to SHG intensity proportional to the square of the applied static electric field strength

$$I_{\text{SHG}} \sim |\chi_{\text{quasi}}^{(2)}|^2 \sim E_{\text{DC}}^2 \quad (2)$$

Such a typical EFISH response curve is shown in **Figure 5**.

In contrast to Equation (1), the minimum of the SHG intensity is not at  $E_{\text{DC}} = 0 \text{ V m}^{-1}$ . This can be explained by describing the total  $\chi^{(2)}$  as the sum of the quasi- $\chi^{(2)}$  of the EFISH effect and field-free bulk  $\chi^{(2)}$  of the material (see Section 3.1)

$$\chi_{\text{total}}^{(2)} = \chi_{\text{bulk}}^{(2)} + \chi_{\text{quasi}}^{(2)} \quad (3)$$

Since the sign of the quasi- $\chi^{(2)}$  depends on the sign of  $E_{\text{DC}}$ , both parts of the total  $\chi^{(2)}$  can sum up (equal signs of  $\chi_{\text{bulk}}^{(2)}$  and

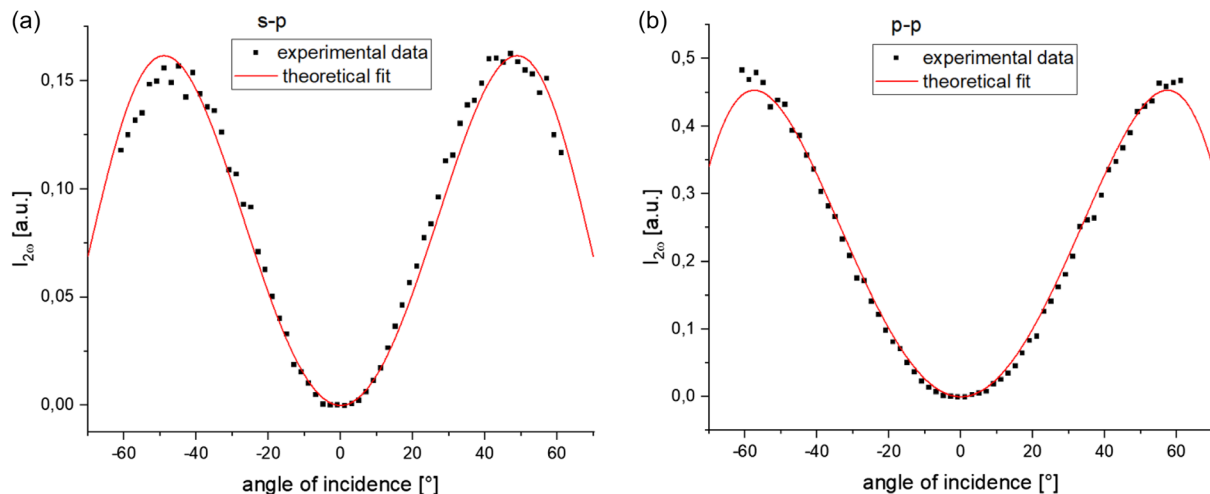


**Figure 4.** Measured SHG intensities depending on the angle of incidence for a) s-p configuration and b) p-p configuration. Fits according to Equation (5).

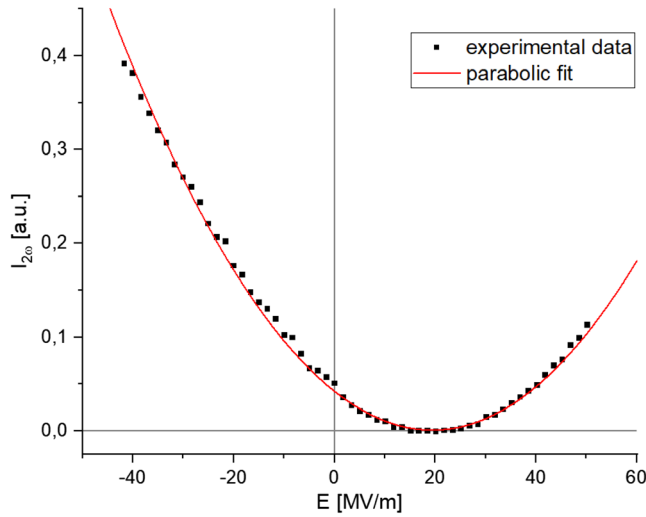


**Figure 5.** Measured SHG intensity depending on the applied static electric field strength. Fit according to Equation (2).

$\chi_{\text{quasi}}^{(2)}$  or counteract (different signs). If  $\chi_{\text{bulk}}^{(2)}$  and  $\chi_{\text{quasi}}^{(2)}$  counteract, the minimum of  $I_{\text{SHG}}$  is found where both balance each other out

$$|\chi_{\text{bulk}}^{(2)}| = |\chi_{\text{quasi}}^{(2)}| \quad (4)$$

## 4. Evaluation

### 4.1. Determination of $\chi^{(2)}$ Tensor Components

To evaluate the data from the field-free SHG measurements and to determine the effective  $\chi^{(2)}$  values, an air–film–substrate–air model suggested by Herman and Hayden is applied, which describes the transmitted SHG intensity  $I_{2\omega}$  from a thin film by<sup>[25]</sup>

$$I_{2\omega}(\theta) = \frac{128\pi^3}{c} \frac{(t_{\text{af}}^{\omega})^4 (t_{\text{fs}}^{2\omega})^2 (t_{\text{sa}}^{2\omega})^2}{(n_{2\omega} \cos \theta_{2\omega})^2} \left( \frac{2\pi L}{\lambda} \right)^2 I_{\omega}^2 (\chi_{\text{eff}}^{(2)})^2 \times \frac{\sin^2(\psi) + \sinh^2(\delta_{\omega} - \delta_{2\omega})}{\psi^2 + (\delta_{\omega} - \delta_{2\omega})^2} \exp(-2(\delta_{\omega} + \delta_{2\omega})) \quad (5)$$

$t_{\text{af}}^{\omega}$ ,  $t_{\text{fs}}^{2\omega}$ , and  $t_{\text{sa}}^{2\omega}$  are standard Fresnel transmission coefficients, which are frequency, polarization, and angle dependent. They describe the transmission at the air–film (af), film–substrate (fs), and substrate–air (sa) interface, respectively.  $n_{2\omega}$  is the refractive index of the film at frequency  $2\omega$ ,  $L$  is the thickness of the film,  $I_{\omega}$  is the intensity of the fundamental beam at the sample surface, and  $\chi_{\text{eff}}^{(2)}$  is the effective second-order susceptibility value of the investigated film (see Equation (9) and (10)). Furthermore, the  $\delta$ 's and the  $\psi$  are related to absorption and phase mismatch between fundamental and SHG beam within the film, respectively. Here the relations are

$$\psi = \frac{2\pi L}{\lambda} (n_{\omega} \cos \theta_{\omega} - n_{2\omega} \cos \theta_{2\omega}) \quad (6)$$

$$\delta_{\omega} = \frac{2\pi L}{\lambda} \frac{\kappa_{\omega}}{\cos \theta_{\omega}} \quad (7)$$

and

$$\delta_{2\omega} = \frac{2\pi L}{\lambda} \frac{\kappa_{2\omega}}{\cos \theta_{2\omega}} \quad (8)$$

where the  $\kappa$ 's are the imaginary parts of the refractive index at the frequencies  $\omega$  and  $2\omega$ . As Equation (6) shows, the value of  $\psi$  depends on the dispersion of the material and the angle of incidence. Therefore, the term in Equation (5) containing  $\psi$  gives rise to the Maker fringe patterns, which can be seen for large angle of incidence in Figure 4a,b. The measured SHG intensities are compared via Equation (5) to the SHG response of a phase-matched BBO crystal with a thickness of 10  $\mu\text{m}$  and a known  $\chi^{(2)}$  value. This results in angle-dependent effective  $\chi^{(2)}$  values of the investigated films. A typical dataset is shown in Figure 6.

Since we already know that the films exhibit a  $C_{\infty v}$  symmetry, we can describe the measured effective  $\chi^{(2)}$  values for s–p and p–p polarization configuration by<sup>[26]</sup>

$$\text{s-p: } \chi_{\text{eff}}^{(2)} = \chi_{\text{zxx}}^{(2)} \sin \theta_{2\omega} \quad (9)$$

$$\text{p-p: } \chi_{\text{eff}}^{(2)} = \chi_{\text{xxx}}^{(2)} \sin 2\theta_{\omega} \cos \theta_{2\omega} + \sin \theta_{2\omega} (\chi_{\text{xxx}}^{(2)} \cos^2 \theta_{\omega} + \chi_{\text{zzz}}^{(2)} \sin^2 \theta_{\omega}) \quad (10)$$

For symmetry group  $C_{\infty v}$  it applies that  $\chi_{\text{xxx}}^{(2)} = \chi_{\text{zxx}}^{(2)} = \chi_{\text{yyz}}^{(2)} = \chi_{\text{zyy}}^{(2)}$  and  $\chi_{\text{zxx}}^{(2)} = \chi_{\text{zyy}}^{(2)}$  while all other tensor components apart from  $\chi_{\text{zzz}}^{(2)}$  vanish. The notation we use here includes  $x$  and  $y$  as two orthogonal in-plane directions and  $z$  as the film normal. By fitting the angle-dependent effective  $\chi^{(2)}$  values according to Equation (9) and (10) (see Figure 6a,b), we can extract the non-vanishing tensor components  $\chi_{\text{xxx}}^{(2)}$ ,  $\chi_{\text{zxx}}^{(2)}$ , and  $\chi_{\text{zzz}}^{(2)}$  from our measurements. The results for the main component  $\chi_{\text{zzz}}^{(2)}$  depending on the refractive index of the material at 1030 nm wavelength are shown in Figure 7. The margin of error for  $\chi^{(2)}$  is  $\pm 13\%$ , arising from fluctuations of the intensity of the input beam ( $\pm 5\%$ ), noises and counting errors of the photomultiplier tube (PMT) ( $\pm 10\%$ ), and inhomogeneity of the deposited film thickness ( $\pm 5\%$ ). For  $\chi_{\text{xxx}}^{(2)}$  and  $\chi_{\text{zxx}}^{(2)}$  the results can be found in the Supplement 1. Note that for refractive indices larger than  $\approx 2.1$ , the increase of  $\chi_{\text{zzz}}^{(2)}$  depending on the refractive index exceeds Miller's rule (see Supplement 1).<sup>[27]</sup>

To confirm that the SHG signal has a bulk and not a surface origin, we measured the SHG response for different layer thicknesses of the PECVD-grown materials. The result for silicon nitride and silicon oxide is shown in Figure 8. The fact that the measured SHG intensity rises with the square of the layer thickness  $L$  is typical for a bulk response. This is shown in Figure 8 by fitting the data to

$$I_{\text{SHG}} \sim L^2 \quad (11)$$

The results for the silicon nitride samples we obtained from the free-space SHG measurements match very well with the  $\chi^{(2)}$  values given in the literature.<sup>[6]</sup> Yet an explanation for this bulk  $\chi^{(2)}$  is still pending.

Table 1 presents an overview of the main components of  $\chi^{(2)}$  of silicon nitride reported in the literature up to now, including

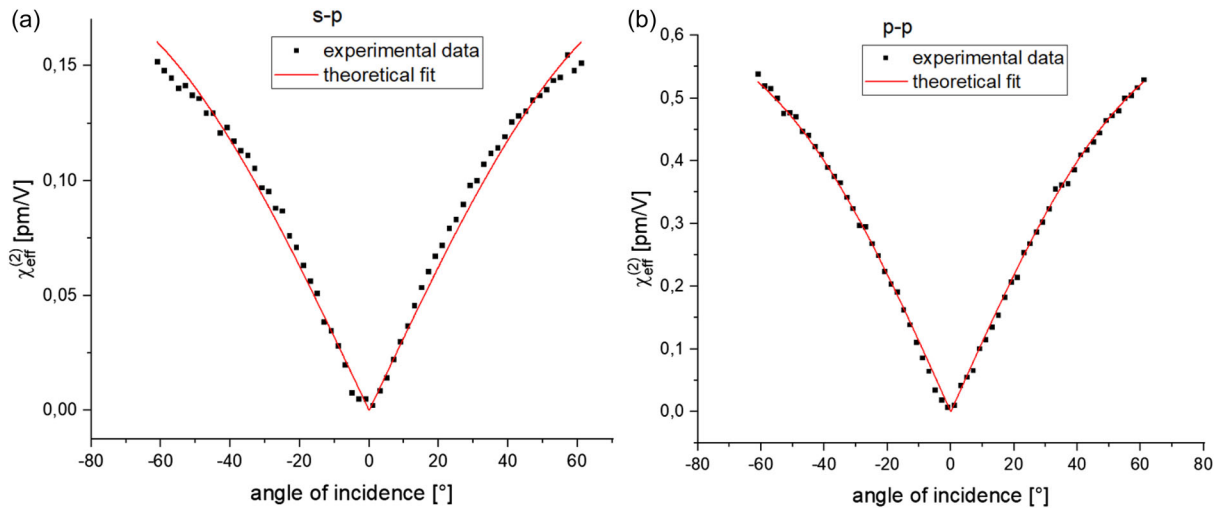


**Figure 6.** The intensities of Figure 4 are translated into  $\chi_{\text{eff}}^{(2)}$  values by Equation (5) and shown here in diagram a,b), respectively. Fits according to Equation (9) and (10), respectively.

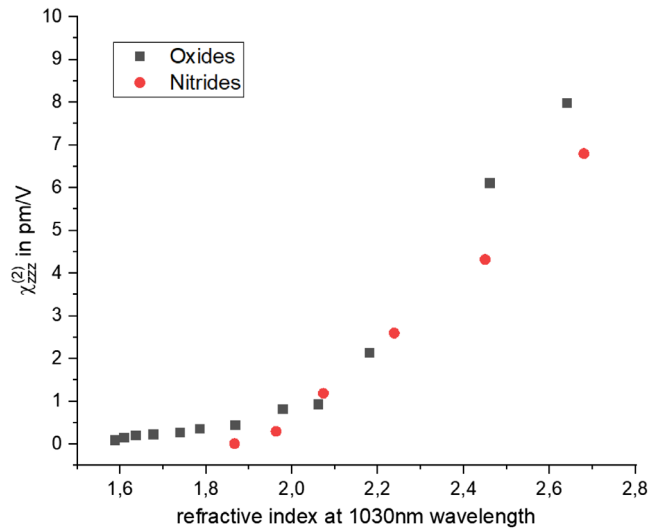


**Figure 7.** Determined main components of the field-free  $\chi^{(2)}$  tensor depending on the refractive index at 1030 nm of the different silicon nitrides (red) and silicon oxides (grey).

different wavelengths, refractive indices, and deposition methods. Our results (Figure 7) fit well to these reported values. To our knowledge, no  $\chi^{(2)}$  values have been reported in the literature for silicon oxide yet.

#### 4.2. Determination of the $\chi_{zzz}^{(3)}$

To evaluate the EFISH measurements and to determine the main  $\chi^{(3)}$ -tensor components, we first have to transform the measured EFISH intensities (see Figure 5) into voltage-dependent  $\chi_{zzz}^{(2)}$  values (see Figure 9). Since we already determined the field-free bulk  $\chi_{zzz}^{(2)}$  values of the PECVD-grown materials in Section 4.1, we can use these values as the EFISH- $\chi_{zzz}^{(2)}$  values at  $0 \text{ V m}^{-1}$ . This allows an

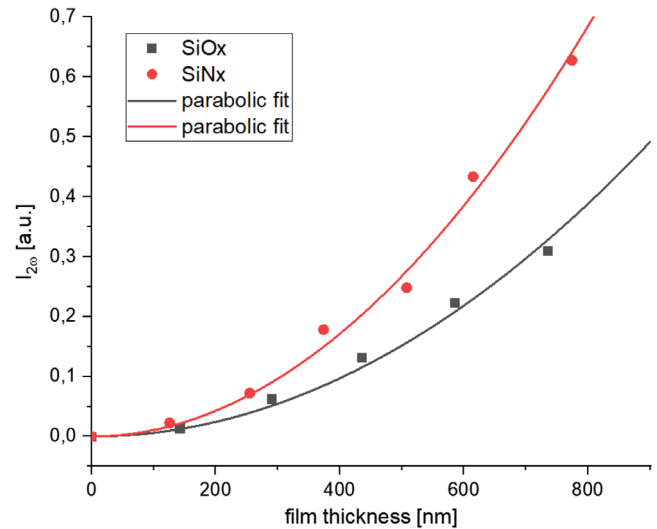


**Figure 8.** SHG intensities measured for films with different thicknesses of silicon nitrides (red) and silicon oxides (grey). Fits according to Equation (11).

easy transformation from voltage-dependent intensities into voltage-dependent  $\chi_{zzz}^{(2)}$  values. As predicted by Equation (1), the EFISH- $\chi_{zzz}^{(2)}$  values exhibit a linear voltage dependency (see Figure 9).

To receive the  $\chi_{zzz}^{(3)}$  values of the investigated materials, the voltage-dependent  $\chi_{zzz}^{(2)}$  values are evaluated according to Equation (1), which gives

$$\left| \frac{d\chi_{zzz}^{(2)}}{dE_{\text{DC}}} \right| = \left| 3\chi_{zzz}^{(3)} \right| \quad (12)$$

Of course, the data can also be evaluated using the minimum of the voltage-dependent  $\chi_{zzz}^{(2)}$  values according to Equation (4), where the following applies

**Table 1.**  $\chi^{(2)}$  main components measured for various silicon nitrides.

$n$	$\chi_{\text{main}}^{(2)}$ [pm V <sup>-1</sup> ]	$\lambda$ [nm]	Deposition method	Year
1.94	2.5	1064	PECVD	2012 <sup>[5]</sup>
2.02	28.6	800	Magnetron sputtering	2013 <sup>[23]</sup>
2.25	68.8	800	Magnetron sputtering	2013 <sup>[23]</sup>
2.35	10.1	800	Magnetron sputtering	2013 <sup>[23]</sup>
1.99	2.4	800	PECVD	2016 <sup>[8]</sup>
1.96	0.3	1550	LPCVD	2017 <sup>[34]</sup>
1.9	0.8	1064	PECVD	2017 <sup>[6]</sup>
2.01	1.7	1064	PECVD	2017 <sup>[6]</sup>
2.17	5.1	1064	PECVD	2017 <sup>[6]</sup>
1.9	2.4	1040	PECVD	2019 <sup>[7]</sup>
2.25	8	1040	PECVD	2019 <sup>[7]</sup>
1.9	0.38	1550	PECVD	2019 <sup>[7]</sup>
2.25	1.25	1550	PECVD	2019 <sup>[7]</sup>
1.87	0.01	1030	PECVD	This work
2.24	2.6	1030	PECVD	This work
2.68	6.8	1030	PECVD	This work

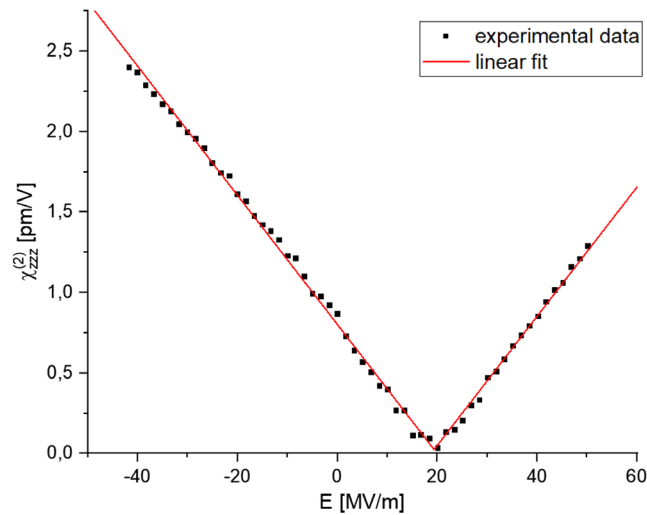


**Figure 9.** Determined main components of the  $\chi^{(2)}$  tensor depending on the applied static electric field strength. Fit according to Equation (1).

$$\left| \chi_{\text{zzz,bulk}}^{(2)} \right| = \left| 3\chi_{\text{zzzz}}^{(3)} E_{\text{min}} \right| \quad (13)$$

Here,  $\chi_{\text{zzz,bulk}}^{(2)}$  is the field-free bulk  $\chi_{\text{zzz}}^{(2)}$  tensor component and  $E_{\text{min}}$  is the applied static electric field strength at the minimum of the voltage-dependent  $\chi_{\text{zzz}}^{(2)}$  values. Both evaluation methods lead to the same results. The determined  $\chi_{\text{zzzz}}^{(3)}$  values of all investigated silicon nitride and silicon oxide films are displayed in the diagram in **Figure 10**. The margin of error for  $\chi_{\text{zzzz}}^{(3)}$  is  $\pm 17\%$ , arising from the uncertainty of  $\chi_{\text{zzz,bulk}}^{(2)}$  ( $\pm 13\%$ ), noises and counting errors of the PMT ( $\pm 10\%$ ), and uncertainty of

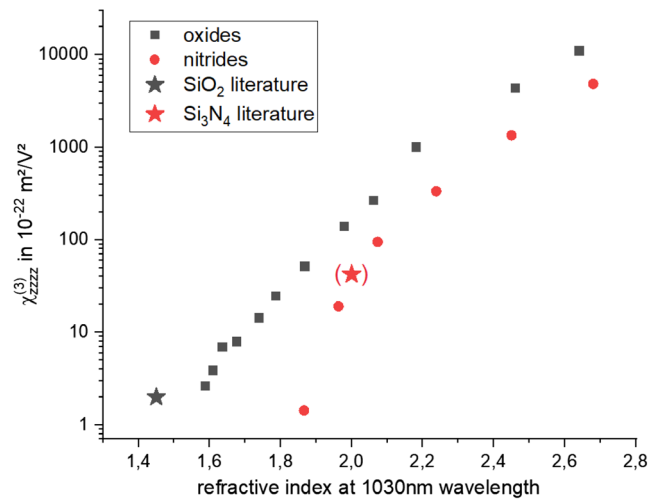


**Figure 10.** Determined  $\chi_{\text{zzzz}}^{(3)}$  values of the silicon nitrides (red) and silicon oxides (gray) depending on the refractive index at 1030 nm wavelength. The stars represent the  $\chi^{(3)}$  values given in the literature for stoichiometric nitride and oxide, respectively. Note that the red star represents the literature value for stoichiometric nitride at 1550 nm wavelength and is therefore put in brackets.

the applied DC field ( $\pm 5\%$ ). Note that the  $\chi^{(3)}$  values of stoichiometric silicon nitride and silicon oxide given in the literature align very well with the measured  $\chi_{\text{zzzz}}^{(3)}$  values in this manuscript.<sup>[20,28–31]</sup>

**Table 2** provides an overview of  $\chi^{(3)}$  and  $n_2$  measurements performed by other groups over the last three decades. It includes different methods such as Z-Scan, self-phase modulation (SPM), FWM, and THG. Our EFISH measurements add a new determination method to this repertoire and deliver complementary and new data, especially for the material platform of silicon oxides.

## 5. Discussion

By conducting free-space SHG measurements, we observed a surprising field-free bulk  $\chi^{(2)}$  in silicon oxides, as large as the well-known bulk  $\chi^{(2)}$  in silicon nitrides. For both material platforms, the main component of the  $\chi^{(2)}$ -tensor significantly increases with rising silicon content and a corresponding higher refractive index. For refractive indices larger than 2.4, the  $\chi^{(2)}$  main component of both materials exceeds that of traditional nonlinear crystals such as BBO.<sup>[32]</sup> For silicon oxides, the field-free bulk  $\chi_{\text{zzz}}^{(2)}$  could be increased by a factor of  $\approx 80$  between the sample with the lowest refractive index and the sample with the highest refractive index. The nitrides show a field-free bulk  $\chi_{\text{zzz}}^{(2)}$  enhancement of a factor of  $\approx 23$  between stoichiometric nitride and the SRN with the highest refractive index. This demonstrates a widely tunable and controllable optical second-order nonlinearity by material composition in both material platforms. Furthermore, the  $\chi_{\text{zzz}}^{(2)}$  can be additionally tuned by applying a static electric field (EFISH effect). The strength of this effect



**Table 2.**  $\chi^{(3)}$  and  $n_2$  values measured for various silicon nitrides and silicon oxides in chronological order.

Material	$n$	$\chi^{(3)} \times 10^{-19} \text{ m}^2 \text{ V}^{-2}$	$n_2 \times 10^{-13} \text{ cm}^2 \text{ W}^{-1}$	$\lambda [\text{nm}]$	Deposition method	Measurement method	Year
SiN <sub>x</sub>	1.91	–	0.024	1548	PECVD	Kerr	2008 <sup>[28]</sup>
SiN <sub>x</sub>	1.96	–	0.009	1550	LPCVD	SPM	2010 <sup>[29]</sup>
SiN <sub>x</sub>	–	–	10 000	800	Magnetron sputtering	Z-Scan	2012 <sup>[24]</sup>
SiN <sub>x</sub>	–	–	400 000	1400	Magnetron sputtering	Z-Scan	2012 <sup>[24]</sup>
SiN <sub>x</sub>	–	28.4	20	1064	Magnetron sputtering	Z-Scan	2017 <sup>[35]</sup>
SiN <sub>x</sub>	–	89	62.7	1550	Magnetron sputtering	Z-Scan	2017 <sup>[35]</sup>
SiN <sub>x</sub>	2.01	–	0.025	1550	PECVD	FWM	2017 <sup>[12]</sup>
SiN <sub>x</sub>	2.49	–	0.16	1550	PECVD	FWM	2017 <sup>[12]</sup>
SiN <sub>x</sub>	2.71	–	0.21	1550	PECVD	FWM	2017 <sup>[12]</sup>
SiN <sub>x</sub>	2.01	–	0.07	1550	PECVD	FWM	2018 <sup>[20]</sup>
SiN <sub>x</sub>	1.99	–	0.056	1550	Magnetron sputtering	FWM	2020 <sup>[30]</sup>
SiN <sub>x</sub>	2.5	1.56	125	1550	PECVD	FWM	2024 <sup>[16]</sup>
SiN <sub>x</sub>	3.2	12.6	76	1550	PECVD	FWM	2024 <sup>[16]</sup>
SiN <sub>x</sub>	1.96	0.02	0.014	1030	PECVD	EFISH	This work
SiN <sub>x</sub>	2.24	0.34	0.19	1030	PECVD	EFISH	This work
SiN <sub>x</sub>	2.68	4.9	1.91	1030	PECVD	EFISH	This work
SiO <sub>2</sub>	1.45	0.002	–	1064	Fused silica	THG	2000 <sup>[31]</sup>
SiO <sub>x</sub>	–	–	35 000	800	Magnetron sputtering	Z-Scan	2012 <sup>[24]</sup>
SiO <sub>2</sub>	1.45	–	0.0022	1030	Fused silica	SPM	2019 <sup>[36]</sup>
SiO <sub>2</sub>	1.45	–	0.0022	1550	Silica glass	SPM	2023 <sup>[37]</sup>
SiO <sub>x</sub>	1.68	0.01	0.008	1030	PECVD	EFISH	This work
SiO <sub>x</sub>	2.06	0.27	0.18	1030	PECVD	EFISH	This work
SiO <sub>x</sub>	2.64	11.1	451	1030	PECVD	EFISH	This work

is related to the third-order nonlinearity of the material. This allows us to determine the  $\chi^{(3)}$  values of the investigated silicon nitrides and silicon oxides. Similar to the bulk  $\chi^{(2)}$  values, the  $\chi^{(3)}$  values are strongly enhanced by increasing the silicon content and the corresponding refractive index. This leads to a  $\chi^{(3)}$  enhancement of a factor  $\approx 100$  from stoichiometric nitride to SRN. For silicon oxide, the enhancement is even stronger with a factor  $\approx 5000$  between stoichiometric oxide and the oxide with the highest silicon content. Comparing the  $\chi^{(3)}$  values of nitrides and oxides with comparable refractive indices, it can be seen that the  $\chi^{(3)}$  of the oxides exceeds that of the nitrides by at least a factor 2. This makes silicon oxide an even more effective EFISH material than silicon nitride.

## 6. Conclusion

In summary, this work provides an overview over the optical second- and third-order nonlinearities of PECVD-grown silicon nitrides and silicon oxides. PECVD-grown nonstoichiometric silicon oxides, alongside the well-known PECVD-grown nonstoichiometric silicon nitrides, are introduced as promising candidates for nonlinear electro-optic applications on chip due to their CMOS compatibility and the enhanced and widely tunable optical second- and third-order nonlinearities.

## Supporting Information

Supporting Information is available from the Wiley Online Library or from the author.

## Acknowledgements

The authors acknowledge financial assistance with the publication costs within the framework of the DEAL agreement.

## Conflict of Interest

The authors declare no conflict of interest.

## Author Contributions

**Laurids Wardenberg:** Conceptualization (lead); Data curation (lead); Formal analysis (lead); Investigation (lead); Writing—original draft (lead). **André Kühling:** Data curation (supporting); Formal analysis (supporting); Investigation (equal). **Jörg Schilling:** Conceptualization (equal); Resources (lead); Supervision (lead); Writing—review & editing (lead).

## Data Availability Statement

The data that support the findings of this study are available from the corresponding author upon reasonable request.

## Keywords

electric field-induced second-harmonic generations, nonlinear optics, plasma-enhanced chemical vapor depositions, second-order nonlinearities, silicon nitrides, silicon oxides, third-order nonlinearities

Received: August 16, 2024

Revised: November 13, 2024

Published online: November 26, 2024

- [1] D. J. Blumenthal, R. Heideman, D. Geuzebroek, A. Leinse, C. Roeloffzen, in *Proc. of the IEEE*, IEEE, Aachen, Germany **2018**.
- [2] C. Xiang, W. Jin, J. E. Bowers, *Photonics Res.* **2022**, *10*, A82.
- [3] X. Wang, P. Ji, S. Li, F. Wang, H. Deng, S. Yang, *Meas. Sci. Technol.* **2024**, *35*, 055201.
- [4] W. Jin, R. G. Polcawich, P. A. Morton, J. E. Bowers, *Opt. Express* **2018**, *26*, 3174.
- [5] T. Ning, H. Pietarinen, O. Hyvärinen, J. Simonen, G. Genty, M. Kauranen, *Appl. Phys. Lett.* **2012**, *100*, 161902.
- [6] K. Koskinen, R. Czaplicki, A. Slablab, T. Ning, A. Hermans, B. Kuyken, V. Mitta, G. S. Murugan, T. Niemi, R. Baets, M. Kauranen, *Opt. Lett.* **2017**, *42*, 5030.
- [7] H.-H. Lin, R. Sharma, A. Friedman, B. M. Crome, F. Vallini, M. W. Puckett, K. Kieu, Y. Fainman, *APL Photonics* **2019**, *4*, 036101.
- [8] M. W. Puckett, R. Sharma, H.-H. Lin, M.-H. Yang, F. Vallini, Y. Fainman, *Opt. Express* **2016**, *24*, 16923.
- [9] F. Karouta, K. Vora, J. Tian, C. Jagadish, *J. Phys. D: Appl. Phys.* **2012**, *45*, 445301.
- [10] I. Guler, *Mater. Sci. Eng. B* **2019**, *246*, 21.
- [11] C.-H. Cheng, C.-S. Fu, H.-Y. Wang, S. Y. Set, S. Yamashita, G.-R. Lin, *APL Photonics* **2022**, *7*, 081101.
- [12] C. Lacava, S. Stankovic, A. Z. Khokhar, T. D. Bucio, F. Y. Gardes, G. T. Reed, D. J. Richardson, P. Petropoulos, *Sci. Rep.* **2017**, *7*, 22.
- [13] D. T. H. Tan, K. J. A. Ooi, D. K. T. Ng, *Photonics Res.* **2018**, *6*, B50.
- [14] B.-U. Sohn, J. W. Choi, D. K. T. Ng, D. T. H. Tan, *Sci. Rep.* **2019**, *9*, 10364.
- [15] A. Friedman, H. Nejadriahi, R. Sharma, Y. Fainman, *Opt. Lett.* **2021**, *46*, 4236.
- [16] D. Belogolovskii, N. Alic, A. Grieco, Y. Fainman, *Adv. Photonics Res.* **2024**, *5*, 2400017.
- [17] Y. Cao, B.-U. Sohn, H. Gao, P. Xing, G. F. R. Chen, D. K. T. Ng, D. T. H. Tan, *Sci. Rep.* **2022**, *12*, 9487.
- [18] N. M. Hanh Duong, G. Saerens, F. Timpu, M. T. Buscaglia, V. Buscaglia, A. Morandi, J. S. Müller, A. Maeder, F. Kaufmann, A. S. Solntsev, R. Grange, *Opt. Mater. Express* **2022**, *12*, 3696.
- [19] M. Akbari, A. A. Kalachev, *Laser Phys. Lett.* **2016**, *13*, 115204.
- [20] L. Wang, W. Xie, D. van Thourhout, Y. Zhang, H. Yu, S. Wang, *Opt. Express* **2018**, *26*, 9645.
- [21] J. S. Levy, M. A. Foster, A. L. Gaeta, M. Lipson, *Opt. Express* **2011**, *19*, 11415.
- [22] K. J. A. Ooi, D. K. T. Ng, T. Wang, A. K. L. Chee, S. K. Ng, Q. Wang, L. K. Ang, A. M. Agarwal, L. C. Kimerling, D. T. H. Tan, *Nat. Commun.* **2017**, *8*, 13878.
- [23] E. F. Pecora, A. Capretti, G. Miano, L. Dal Negro, *Appl. Phys. Lett.* **2013**, *14*, 141114.
- [24] S. Minissale, S. Yerci, L. Dal Negro, *Appl. Phys. Lett.* **2012**, *100*, 021109.
- [25] W. N. Herman, L. M. Hayden, *J. Opt. Soc. Am. B* **1995**, *12*, 416.
- [26] R. L. Sutherland, in *Handbook of Nonlinear Optics*, Marcel Dekker, New York **2003**.
- [27] R. W. Boyd, in *Nonlinear Optics*, Academic Press, Rochester, NY, USA **2008**.
- [28] K. Ikeda, R. E. Saperstein, N. Alic, Y. Fainman, *Opt. Express* **2008**, *16*, 12987.
- [29] M.-C. Tien, J. F. Bauters, M. J. R. Heck, D. J. Blumenthal, J. E. Bowers, *Opt. Express* **2010**, *18*, 23562.
- [30] A. Frigg, A. Boes, G. Ren, T. G. Nguyen, D.-Y. Choi, S. Gees, D. Moss, A. Mitchell, *APL Photonics* **2020**, *5*, 011302.
- [31] U. Gubler, C. Bosshard, *Phys. Rev. B* **2000**, *61*, 10702.
- [32] I. Shoji, H. Nakamura, K. Ohdaira, T. Kondo, R. Ito, T. Okamoto, K. Tatsuki, S. Kubota, *J. Opt. Soc. Am. B* **1999**, *16*, 620.
- [33] L. Wardenberg, B. Bunk, G. von Freymann, J. Schilling, *Opt. Express* **2024**, *32*, 23856.
- [34] A. Billat, D. Grassani, M. H. P. Pfeiffer, S. Kharitonov, T. J. Kippenberg, C.-S. Brès, *Nat. Commun.* **2017**, *8*, 1016.
- [35] B. Ding, X. Yu, H. Lu, X. Xiu, C. Zhang, C. Yang, S. Jiang, B. Man, T. Ning, Y. Huo, *J. Appl. Phys.* **2019**, *125*, 113102.
- [36] P. Kabaciński, T. M. Kardaś, Y. Stepanenko, C. Radzewicz, *Opt. Express* **2019**, *27*, 11018.
- [37] R. Schiek, *Opt. Mater. Express* **2023**, *13*, 1727.